



HAL
open science

Fragmentation and coalescence dynamics of non-wetting blobs during immiscible two-phase flows in porous media

Laurent Talon, R. Bouguemari, A. Yiotis, Dominique Salin

► To cite this version:

Laurent Talon, R. Bouguemari, A. Yiotis, Dominique Salin. Fragmentation and coalescence dynamics of non-wetting blobs during immiscible two-phase flows in porous media. *Physical Review Fluids*, 2023, 8 (9), pp.093602. 10.1103/PhysRevFluids.8.093602 . hal-04441214

HAL Id: hal-04441214

<https://universite-paris-saclay.hal.science/hal-04441214>

Submitted on 6 Feb 2024

HAL is a multi-disciplinary open access archive for the deposit and dissemination of scientific research documents, whether they are published or not. The documents may come from teaching and research institutions in France or abroad, or from public or private research centers.

L'archive ouverte pluridisciplinaire **HAL**, est destinée au dépôt et à la diffusion de documents scientifiques de niveau recherche, publiés ou non, émanant des établissements d'enseignement et de recherche français ou étrangers, des laboratoires publics ou privés.

Fragmentation and coalescence dynamics of non-wetting blobs during immiscible two-phase flows in porous media

L. Talon,¹ R. Bouguemari,¹ A. Yiotis,² and D. Salin¹

¹*Université Paris-Saclay, CNRS, FAST, 91405, Orsay, France*

²*School of Mineral Resources Engineering, Technical University of Crete, 73100 Chania, Greece*

We study experimentally the dynamics of non-wetting blobs flowing simultaneously with a wetting fluid in a quasi-two-dimensional porous medium consisting of random obstacles. The blobs continuously merge forming larger ones (coalescence) and breakup into smaller ones (fragmentation) leading to an overall dynamic equilibrium between the two processes. We develop a clustering algorithm for the identification of fragmentation and coalescence events that records the size of the blobs prior and immediately after each event from high-resolution videos of the immiscible flow experiments. The results provide significant insight on the main physical features of these two processes, such as blob size distributions, breakup and coalescence frequency as a function of total flow rate, and the size distributions of the blobs formed by either the fragmentation or coalescence of other ones. One of the salient features of the fragmentation process in our study is that blobs smaller than the typical pore size exhibit a higher probability of producing two almost identical children (in size), whereas larger blobs breakup into two children of different sizes. In the latter case, one of children is found to have a dimension practically equal to the typical pore size. Our experimental results are also interpreted in the framework of a mean-field approach, where the dynamics of the blob sizes is expressed through an integro-differential population balance equation (PBE) that comprise terms for the description of the rates of size gains and losses by either fragmentation or coalescence. We recover appropriate expressions for the relevant coalescence and fragmentation kernels, as functions of the blob sizes that participate in each event. A rather surprising result is that for a given blob size population, we obtain an equilibrium between the gains by fragmentation and the losses by coalescence. Furthermore, the opposite is also true, as the population gains by coalescence are found to be equal to the losses by fragmentation.

I. INTRODUCTION

Many natural and industrial processes involve two-phase flows in porous media. Examples include air and water flow in soils, oil and natural gas recovery from hydrocarbon reservoirs, CO₂ sequestration, etc. Such processes have been the subject of considerable research in order to provide physical insight on the dominant transport mechanisms under various flow conditions. More specifically, two-phase subsurface flows are traditionally modeled at the Representative Elementary Volume (REV) scale, where the porous medium is treated as an effective continuum and the volumetric flux of each phase is related to pressure gradients through experimentally determined parameters. The most commonly used approach relies on a generalization of Darcy's law that leads to a linear relationship between the flow rate and the pressure gradient for each phase:

$$\vec{q}_1 = \frac{\kappa k_1(S)}{\mu_1} \vec{\nabla} P_1, \quad \vec{q}_2 = \frac{\kappa k_2(S)}{\mu_2} \vec{\nabla} P_2, \quad (1)$$

where κ is the intrinsic permeability of the medium, q_α , P_α , μ_α are respectively the flow rate, pressure and dynamic viscosity of the α phase and S the saturation of the non-wetting phase. The prefactors $k_\alpha(S)$ are the relative permeabilities of each phase that are typically expressed as a function of saturation.

One of the main underlying assumptions leading to this expression is that each phase are continuous over the entire porous domain in order to define a corresponding continuous pressure field for each one. While such an approach has proven to be adequate for the description of subsurface flows at the field scale, there are also situations where this approach is not valid because one of the phases is not connected. For example, Hilfer[1] proposed an extension of the classical relative permeability formalism that takes into account the coexistence and the flow coupling between a connected and a disconnected phase. In the specific case when the disconnected phase is the non-wetting one, then it flows in the form of blobs and a noticeable deviation from the relative permeability approach is observed, as the flow curve exhibits a nonlinear regime due to the progressive mobilization of blobs at higher flow rates[2–7]. The characterisation of the distribution of the phases, especially the unconnected ones, is therefore crucial for the improvement of the description of the flow at a large scale.

A. Blob size distribution

When one of the phases is disconnected, it seems fairly intuitive that the flow dynamics of the blobs depends on their size. In particular, the presence of such blobs in the pore space implies that a minimum pressure gradient should be imposed in order to overcome pore-scale capillary forces and mobilize them. The mobilization conditions for stranded blobs has been a subject of several studies [8–10]. The early

work of Ng et al.[8] first showed the correlation between the blob size and its mobilization conditions. In addition, Wardlaw and Mckellar [11] identified that the mobilization of larger blobs requires their fragmentation into smaller pore-sized blobs ("singlets"). We note, however, that this mechanism has not been observed in more recent experiments [12]. Apparently, very small blobs with sizes less than that of the typical pore size are not subjected to capillary forces and they flow along the dominant flow paths. This situation was termed as Drop Traffic Flow (DTF) by Avraam and Payatakes[13]

Several studies have proposed that the blob size distribution $n(s)$ follows a power law as follows[2, 4, 14–16];

$$n(s) \propto s^{-\tau}. \quad (2)$$

where s is the blob size. This behavior has been explained theoretically in the context of percolation theory and related models [16–19]. To briefly recall the invasion percolation model: for an imposed pressure difference ΔP , one distinguish between "active" and "inactive" pores, for which ΔP is respectively higher or lower than the local capillary pressure. For a given entry pressure ΔP , all "active" pores connected to the entrance are invaded. The remaining wetting fluid is then dispatched in clusters, whose size distribution follows a power law with a universal exponent $\tau \simeq 2.05$ in 2D and $\tau = 2.18$ in 3D [20]. However, the experimental verification of this universal law has been a subject of active debate, since several studies verify the above scaling and exponents (e.g. [2, 4]), while others propose different values for τ (e.g. [11, 21]). There are even recent experimental studies where the power-law scaling is not even obvious (e.g. [12, 22]).

There are several possible explanations for the divergence of literature results from the percolation theory. One possible explanation should be attributed to the differences among experimental protocols. For example, the injection of the non-wetting phase by an invasion front or by the simultaneous co-injection of the two phases could lead to different configurations. The percolation model would be more suitable for the description of the first case. Furthermore, the percolation model corresponds essentially to a quasi-static flow condition, that does not account (at least in its basic formulation) for the effects of viscous stresses on the dynamics of mobile blobs, especially at high flow rates.

Another possibility is that the percolation theory lies on a quasi-static assumption, and thus does not account for some phenomena that might be important at high flow conditions. In particular, the two phases might fragment or coalesce which can potentially modify the blob size distribution. In this direction, a modified percolation model that takes this aspect into account has been proposed by Meakin et al. [16]. This study proposes a different scaling exponent than that of ordinary percolation. In addition, recent μ -CT (micro computed tomography) experiments and numerical simulations at the pore-scale [3, 23, 24] highlight the important effects of blob fragmentation, as well of blob coalescence in

two-phase flow dynamics.

B. Blob Fragmentation Dynamics

Blob fragmentation in porous media is a process that has been greatly studied in the literature. In their study, Payatakes and Dias [15] identified three dominant mechanisms of fragmentation. The first mechanism is the snap-off process proposed by Roof [25] which occurs when the non-wetting phase passes through a constriction (i.e. a pore throat). As the tip of the blob exits the throat in the downstream direction, the radius of curvature of the interface increases and, as a consequence, the capillary pressure at the tip decreases. At some point, the pressure within the blob region that still lies in the throat may become higher than the pressure at the downstream tip, thus causing the blob to break up. This mechanism is quasi-static and depends only on the geometry of the restriction (i.e. there is no flow threshold for this fragmentation mechanism)

The second mechanism is that of "pinch off", that corresponds to the instability of an infinite fluid thread in another fluid, as described by Plateau [26] and Rayleigh [27]. Here, the stability criterion is also independent of the flow rate. The average speed only affects the growth rate [28].

The final mechanism is the "dynamic break-up", that occurs when a blob encounters a bifurcation path. In this case, a blob reaches a solid obstacle where it will follow either of the two available flow paths, or it will deform and break-up to invade both, as the movement of its central part is constrained by a solid obstacle. This mechanism has been studied recently in a microfluidic device by Salkin *et al.* [29] and Protière *et al.* [30]. In both studies, the authors showed the existence of a critical capillary number (ratio of viscous forces to interfacial tension) that results in fragmentation. In porous media, [12] and [7] also proposed a critical capillary number for the onset of fragmentation.

We first remark that these blob fragmentation mechanisms depend differently on the average flow rate (capillary number). A threshold capillary number is for instance required for "dynamic break-up", while the "snap-off" and "pinch-off mechanisms" occur in under quasi-static conditions, and are thus independent of the capillary number. However, in all cases, the average flow rate affects the velocity of the blob, which determines the speed at which the blob will encounter obstacles. For this reason, it is expected that the average flow rate will increase the breakup frequency for any mechanisms.

The second remark is that, for all the mechanisms, the criteria for break-up depends on the geometry and potentially on the local flow rate. Since porous structures are generally heterogeneous, the pore geometry and local flow are also spatially distributed. The break-up condition must therefore be considered as a spatially heterogeneous variable.

C. Population Balance Equation

From a theoretical point of view, there is a traditional general framework for the study of coalescence and fragmentation (*i.e.* break-up) processes originally proposed by Smoluchowski [31], who derived a mean-field integro-differential population balance equation (PBE) to describe irreversible colloidal coagulation (*i.e.* coalescence). Since then, this approach has been applied to Brownian coagulation, polymer growth [32, 33]. A similar PBE approach has been applied to irreversible fragmentation processes[34]. Combining PBEs for blobs undergoing both fragmentation and coalescence depending on their size and their specific interactions with the sizes of their surrounding blobs, we obtain the following generalized coalescence-fragmentation equation [35–38]:

$$\begin{aligned} \frac{\partial \rho(s)}{\partial t} = & - \int_0^\infty \rho(s, t) \rho(s', t) K(s, s') ds' + \frac{1}{2} \int_0^s \rho(s - s', t) \rho(s', t) K(s - s', s') ds' \\ & - \Gamma(s) \rho(s, t) + \int_s^\infty \beta(s|s') \Gamma(s') \rho(s', t) ds', \end{aligned} \quad (3)$$

where s is the blob size, t is the time, $\rho(s, t)$ is the density number of s -sized blobs at time t , so that $dn(s, t) = \rho(s, t) ds$ is the overall number of blobs with size between s and $s + ds$ at time t . The function $K(s_1, s_2)$ is the collision frequency of a blob of size s_1 (parent 1) with a blob of size s_2 (parent 2). This leads to a larger blob of size $s_1 + s_2$. The function $\Gamma(s)$ is the fragmentation frequency for s -sized blobs[39], while the function $\beta(s|s')$ is the child size distribution, *i.e.* the probability of producing a a blob of size s from the fragmentation of a larger s' -sized blob. As fragmentation produces two children, it is worth mentioning the property $\int_0^{s'} \beta(s|s') ds = 2$.

The first two terms on the right hand side correspond to the loss and gain of blobs of size s due to coalescence, respectively. Indeed, the number of coalescence events involving blobs of sizes between s and $s + ds$ (parent 1) and blobs with size between s' and $s' + ds'$ (parent 2) during the time step dt is:

$$dN^{\text{coal}}(s, s') = \rho(s, t) \rho(s', t) K(s, s') ds ds' dt. \quad (4)$$

More specifically, the first right-hand term represents the probability that a blob of size s coalesces with another blob of any size s' . This results in a net population loss of size s blobs, and is thus integrated over all other sizes, s' from zero to infinite. It should be noted that the number of coalescence should in principle be proportional to the spatial density of blobs (number of blobs per cell area). It follows that the $K(s, s')$ function should probably depend on the cell area considered.

The second term is the probability that a blob of size $s - s' \leq s$ coalesces with another blob of size $s' \leq s$ to produce a child s -sized blob, thus resulting in a net gain of the population of s -sized blobs.

Therefore, this term is integrated over all sizes in $s' \in [0, s]$. The factor $1/2$ takes into account that in the function $K(s, s')$, the parents s and s' are indistinguishable ($K(s, s') = K(s', s)$). Therefore, the same coalescence combination is counted twice in the integral.

The last two terms of eq. (3) correspond to the loss and gain, respectively, of s -sized blobs by fragmentation. The number of fragmentation events for the parent size between s and $s + ds$ during the time step dt is:

$$dN^{\text{frag}}(s) = \Gamma(s)\rho(s, t)dsdt \quad (5)$$

Furthermore, the number of children between s and $s + ds$ created by the fragmentation of a parent of size between s' and $s' + ds'$ during the time step dt is given by:

$$dN_{\text{child}}^{\text{frag}}(s|s') = \Gamma(s')\rho(s')\beta(s|s')dsds'dt \quad (6)$$

$$= dN^{\text{frag}}(s')\beta(s|s')ds \quad (7)$$

Also here, the two children of size s and $s' - s$ are indistinguishable, and thus we have $\beta(s|s') = \beta(s - s'|s')$.

The application of a population balance equation for modeling blob population dynamics in porous media was first proposed by Payatakes et al. [15, 40]. The model was very complex and involved more statistical functions that could be determined either numerically or experimentally using a pore network model [41, 42]. A similar approach was also adopted for modeling foam flow in porous media [43]. In this case, the authors observed only fragmentation events, thus allowing to set $K(s, s') = 0$ in Eq. (3).

Based on the above discussion, it is well evident that the questions concerning blob population dynamics during immiscible two-phase flow in porous media still remain open and challenging. In this work, we thus study experimentally the dynamics of coalescence and fragmentation of blobs under different flow conditions in order to better understand the dynamics of these processes and determine the mean-field functions associated with the Population Balance Equation at steady-state flow conditions. The experiments are performed in a transparent quasi two-dimensional micromodel with stochastically produced solid obstacles [4, 12, 43], that serves as a model porous medium and allows for the optical monitoring and recording of coalescence and fragmentation events. A clustering algorithm is developed for the identification of fragmentation and coalescence events that also allows for measuring the sizes of the involved parent and children blobs, prior and after each event. This approach allows for determining the main characteristics of these processes, including the measurement of the blob size distributions, and the coalescence/fragmentation rates as functions of the total flow rate.

II. EXPERIMENTAL SETUP

The porous domain used in this study is constructed by gluing together two transparent PMMA [poly(methyl methacrylate)] plates of 325 mm length and $b = 120\text{ mm}$ width. The bottom plate is etched using a computer-driven milling machine following a stochastically generated pattern (see [3] for details). This produces obstacles of random size and shape with a typical correlation length of $900\text{ }\mu\text{m}$. The distance between the two surfaces is $e = 300\text{ }\mu\text{m}$ and the top-view porosity is equal to $P = 0.82$. The porous medium is thus a kind of Hele-Shaw cell (two parallel plates separated by a narrow spacing e) with solid obstacles perpendicular to the flow. The typical pore size, i.e., the typical surface area between obstacles is of the order of $s_p \simeq 10\text{ mm}^2$ [4] and the average obstacle size is 1.9 mm^2 . The cell is initially fully saturated by the wetting phase, n-heptane, with a viscosity of $\mu_w = 4.0 \times 10^{-4}\text{ Pa}\cdot\text{s}$. The non-wetting phase is blue dyed water with $\mu_{nw} = 1.0 \times 10^{-3}\text{ Pa}\cdot\text{s}$. The two fluids are co-injected from a single flow inlet at a predefined flow ratio Q_{nw}/Q_w . More details on this experimental setup can be found in [4]. The flow rate can be made non-dimensional by defining a capillary number that represents the ratio of typical viscous forces to capillary forces, $Ca = (\mu_w(Q_w/(be))/\gamma)$ with $\gamma = 5.2 \times 10^{-2}\text{ N/m}$ being the interfacial tension between the two fluids. In our series of experiments, Ca varies from 2×10^{-5} to 1.2×10^{-4} . As mentioned above, some of the basic mechanisms related to fragmentation and coalescence events depend on Ca , while others do not. We therefore use the total flow rate Q , as the characteristic flow parameter. Furthermore, in our experiments we keep flow ratio constant, $Q_w/Q_{nw} = 20$, while varying the total flow rate, $Q = Q_w + Q_{nw}$ in each experiment.

Fig. 1 shows a snapshot of the cell where the transparent solid obstacles are represented in black color, while the non-wetting blobs appear in blue color. The flowing wetting fluid is transparent and completely saturates the remaining pore space. The figure clearly demonstrates the tortuous aspects of the obstacles and the blobs.

During each experiment the pressure difference is measured across the cell in order to determine when a steady state flow condition is reached. This is also confirmed *a posteriori* by checking that the time evolution of the number of blobs does not show any drift (see Appendix). Once the pressure stabilizes, the phase distribution patterns are recorded using a digital camera (Nikon D800) over a field of view further downstream in the cell of size $100\text{ mm} \times 50\text{ mm}$. We record movies for typically 15 min at a rate of 30 frames per second leading to a sequence of about 25000 frames. On each image (time t) we determine the size, s , of each blob leading to the number of blobs between s and $s + ds$ as $dn(s, t) = \rho(s, t)ds$, where $\rho(s, t)$ is the blob size density.

The comparison between an image and either the previous or the next one in time allows to identify both the coalescence and fragmentation events, as well as the sizes of the parents and children involved.

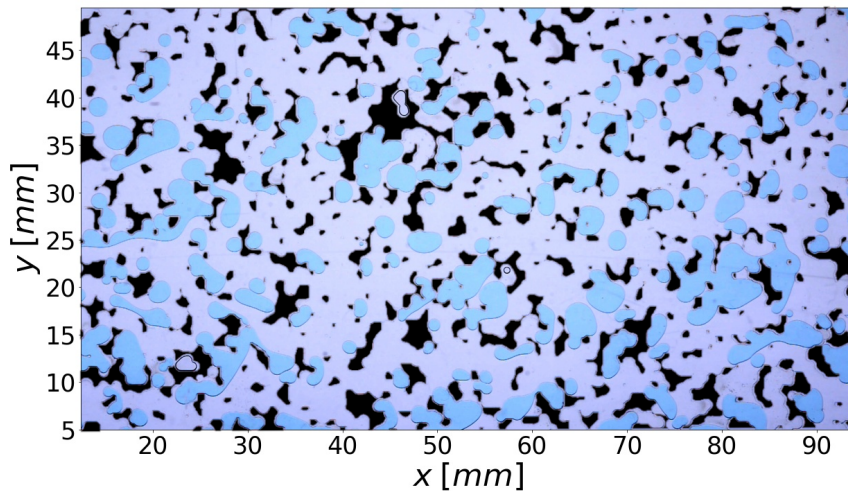


Figure 1. Close-up snapshot of a section of the cell during an immiscible flow experiment. The non-wetting blobs are shown in blue, while the wetting phase is totally transparent. While solid obstacles are also transparent, we represent them here in black color.

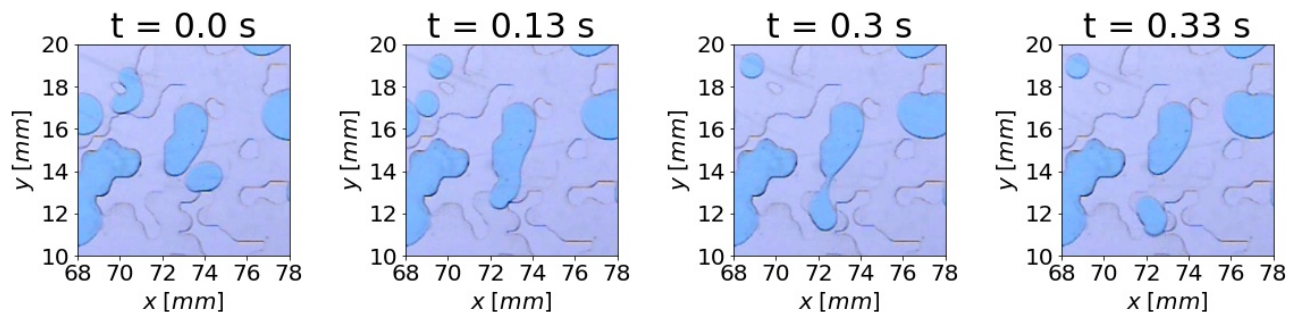


Figure 2. Time sequence of a coalescence event (between $t = 0$ and $t = 0.13$ s) followed by a fragmentation event between $t = 0.3$ s and $t = 0.33$ s

This is achieved using an image-processing algorithm, described in the appendix, that works efficiently as long as the blobs do not move too fast between subsequent images. We are primarily interested here in identifying coalescence event between two parent blobs and fragmentation events resulting to two children blobs. These restrictions impose a sufficiently low flow rate but also a low blob density, so that three blobs do not coalesce between subsequent images. This is the reason why we limit our study to the flow ratio $Q_w/Q_{nw} = 20$. Of course, three-body events are still detected by the algorithm, but their occurrence is quite rare, i.e. less than 5%.

Fig. 2 shows a typical coalescence event that occurs between the two leftmost images (between times 0.0 and 0.13s). This followed by a fragmentation event in the same region shown in the two rightmost images (between times 0.3 and 0.33s). Both events are identified by our algorithm and the sizes of the blobs prior and after the event are recorded.

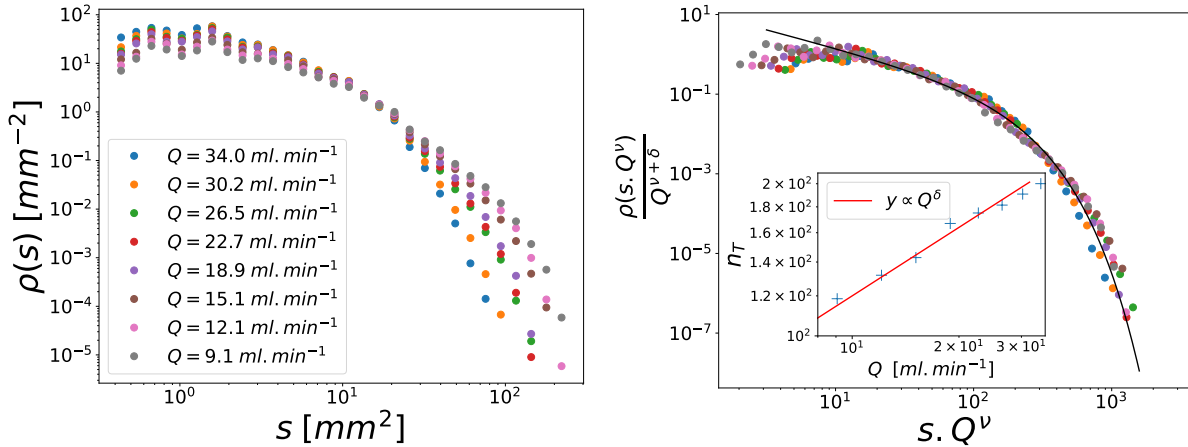


Figure 3. Log-log plot of the stationary blob size density function $\rho(s)$ at different total flow rates Q keeping the ratio of the flow rate of the two fluids constant. On the right, log-log plot of the rescaled density $\rho(s \cdot Q^\nu)/Q^{\nu+\delta}$ versus the rescaled blob size $s \cdot Q^\nu$, with $\nu = 0.7$ and $\delta = 0.45$. The black line corresponds to a fit using a Gamma function $g(x) \propto x^{-0.9}e^{-x/s_0}$. Inset, average number of blob n_T as function of the total flow rate.

III. RESULTS

A. Blob Size Distribution

Under steady state flow conditions we observe that the blob density number $\rho(s, t)$ remains practically constant during the duration of each experiment, meaning that the blob size distribution has reached a steady state. Fig. 3 (left) shows the blob size distribution for different values of the total flow rate Q (for a constant ratio of flow rates of the two fluids $Q_w/Q_{nw} = 20$). The distribution exhibits a slight power-law decay followed by a cutoff s value that decreases with Q . As shown in Fig. 3 (right), all the curves can be fitted very well to a single one using the rescaling:

$$\rho(s) \propto Q^{\delta+\nu} g(sQ^\nu), \quad (8)$$

with $\nu \simeq 0.7 \pm 0.05$ and $\delta \simeq 0.45 \pm 0.05$. It can be deduced from this scaling law that the total number of blobs increases with the total flow rate following $n_T \propto Q^\delta$ (inset of Fig. 3 (right)). This trend is qualitatively expected given that the higher the flow rate, the fragmentation process becomes more pronounced leading to increased blob populations, but also smaller sizes. In addition, we can deduce that the size probability distribution function scales as:

$$\text{Pdf}(s) = \rho(s)/n_T = Q^\nu g(sQ^\nu) \quad \text{with} \quad \nu \simeq 0.7 \pm 0.1. \quad (9)$$

This can be reasonably well fitted by a Gamma function, *i.e.* a power-law with an exponential decay as $g(x) \propto x^{-0.9}e^{-x/s_0}$. Although, the power law is not very obvious because it barely covers an order

of magnitude, the fitting exponent 0.9 ± 0.1 differs significantly from the value of $\tau \simeq 2.05$ which is predicted by the percolation theory. It is interesting to note that an exponent of $\tau \simeq 2$ was measured in a similar experimental configuration by Chevalier et al.[4], but with a different flow condition because only the wetting fluid was injected at the inlet. This finding clearly suggests that the flow conditions have profound impact on the steady-state blob size distribution. It should also be noted that the density of blobs deviates from the gamma distribution for small sizes. In particular, even though the logarithmic plot attenuates it, the density exhibits a maximum around $s \sim 2 \text{ mm}^2$ that is absent from this gamma distribution.

B. Fragmentation dynamics

We now focus on the explicit characteristics of the fragmentation events. Fig. 4 shows a characteristic cloud map of the fragmentation events that occur during the experiment at $Q = 22.7 \text{ ml/min}$. For each dot, x-axis corresponds to the size of the parent blob and the y-axis the size of the children blobs created during this event. Each event is thus represented by two dots (at fixed s_{parent}) that corresponds to the size of the two new blobs. Furthermore, all data points are located below the line $s_{children} = s_{parent}$, given that the size of the children is always $s_{children} < s_{parent}$. Furthermore, the number of events appears to be greater in the center of the diagram, indicating that the number of fragmentation of blob of size s is also proportional to the density of blob $\rho(s)$, which exhibits a maximum.

The fragmentation frequency $\Gamma(s)$ is determined as the number of fragmentation events for each s -sized blob divided by the average number of blobs of this size observed during the recording time, according to eq. (5). Figure 5(left) represents a log-log plot of the calculated fragmentation frequency $\Gamma(s)$ as a function of the parent blob size s for different total flow rates. As expected, the curves demonstrate that fragmentation frequency increases with the flow rate. Furthermore, at fixed Q the frequency also increases significantly with size, meaning that the larger blobs exhibit a higher probability to break-up than smaller ones. It also drops very quickly below a small size $s_c \simeq 0.5 \text{ mm}^2$. Indeed, because of the surface tension and the average size of the obstacles, it is expected that very small droplets never break-up, but rather flow around the obstacles.

We remark that the statistical error of this calculation reduces as the number of blobs increases. Since the blob size density has a maximum, it is therefore expected that the statistical accuracy decreases when the drop size is either very small or very large.

Given the similar shape of the curves, we deduce a scaling law by plotting in Fig. 5(right) the ratio $\Gamma(s)/Q^{\alpha_1}$ as a function of $s - s_c$. The value of s_c , which is assumed to be constant for all flow rates, is obtained by adjustment. A good collapse of the data is thus observed with $\alpha_1 \simeq 1.45 \pm 0.1$ and

$s_c = 0.5 \text{ mm}^2$. This scaling also demonstrates that the fragmentation frequency exhibits two different power laws depending on the blob size. For small sizes, $\Gamma(s)$ follows a power law with an exponent close to two. Beyond a certain blob size, $\Gamma(s)$ still follows a power law but with a smaller exponent. Our results can thus be summarized as follows:

$$\Gamma(s) \propto Q^{\alpha_1} (s - s_c)^{\gamma_1} \quad \text{with} \quad \gamma_1 \simeq 2 \pm 0.3, \quad \text{for} \quad s \lesssim 0.5 \text{ mm}^2 \quad (10)$$

$$\Gamma(s) \propto Q^{\alpha_1} (s - s_c)^{\gamma_2} \quad \text{with} \quad \gamma_2 \simeq 1.1 \pm 0.2, \quad \text{for} \quad s \gtrsim 0.5 \text{ mm}^2 \quad (11)$$

The value of the scaling exponent with respect to the flow rate (i.e. $\alpha_1 \simeq 1.45$) could be explained given that the rate of collisions with obstacles scales with the blob velocity, which is proportional to the total flow rate. Furthermore, if fragmentation results from the competition between viscous stress and capillary force, it would also depend on the mean flow rate through the capillary number Ca [29, 30]. It is thus reasonable to conclude that the fragmentation frequency increases with an exponent greater than 1.

With respect to size scaling, it is worth mentioning that foam fragmentation in a similar apparatus has been reported to yield $\Gamma(s) \propto s^2$ [43, 44]. This observation corresponds very well to our lower size regime, without however the cut-off size. In addition, for larger blob sizes, it can be added that this cut-off size has very little influence on the second scaling law.

From Fig. 4 we can also determine the function $\beta(s|s')$ that represents the probability distribution of children of size s created by the fragmentation of a parent blob of size s' . The functions $\beta(s|s')$ for different flow rates Q are plotted in Fig. 6. As expected, these functions exhibit the symmetry $\beta(s|s') = \beta(s - s'|s')$ as a s -sized parent leads to two children of sizes s and $s' - s$. We also observe that the shape of the distribution of children sizes remains unchanged when varying the total flow rate. However, it changes significantly as a function of parent size. For smaller parents, $\beta(s|s')$ is symmetric with a maximum in the center. This shows that small blobs are more likely to break into two blobs of almost identical size. However, for larger parent blobs, the child distribution exhibits a two-bump shape with a maximum approximately at a constant size $s = s^* \simeq 2 \text{ mm}^2$ and $s = s' - s^*$. The fragmentation of large parent blobs is therefore more prone to lead to children of size s^* and the remaining volume. Again, it is worth mentioning that a similar distribution function for large size has been reported for foam fragmentation [43], but also by Dias *et. al* [41] using a pore network model. In both of these cases, however, the reported distributions had always two bumps.

As with the fragmentation frequency, the distribution of children is thus very different if the size of the parent is smaller or larger than a typical blob size $s^* \simeq 2 - 3 \text{ mm}^2$, which is of the same order as the typical obstacle or pore size. For parent smaller than s^* , the fragmentation is more likely to create two children of equal size. For a parent larger than s^* , fragmentation is more likely to create a child of size

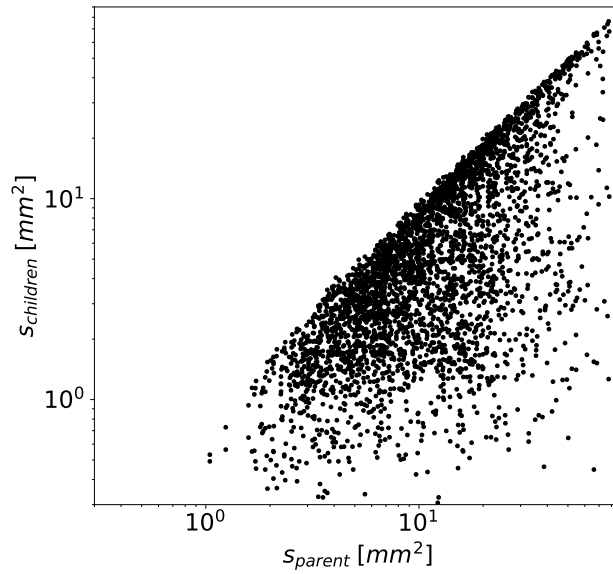


Figure 4. Cloud map of fragmentation events for $Q = 22.7 \text{ ml. min}^{-1}$. Each point corresponds to a child of size $s_{children}$ created by the fragmentation of a parent of size s_{parent} . Therefore, each fragmentation even corresponds to two points in the map. Note that only 2,000 events, out of the total 90,000 fragmentation events of the specific experiments, are shown in the plot for better readability.

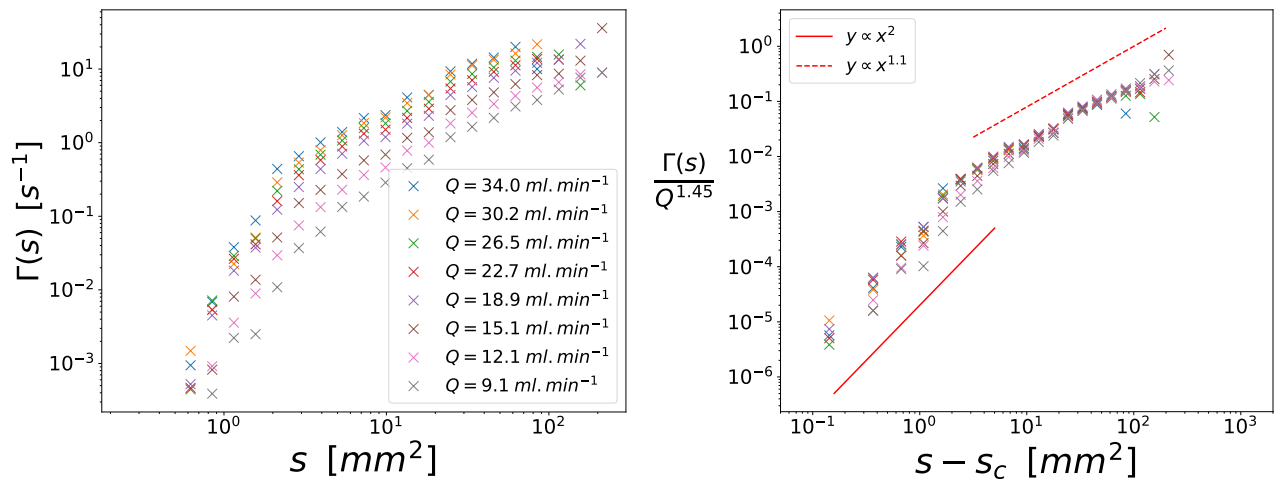


Figure 5. Left: fragmentation frequency as a function of blob size for different flow rates. Right: fragmentation frequency renormalized by the flow rate.

s^* , hence the double peak at fixed size.

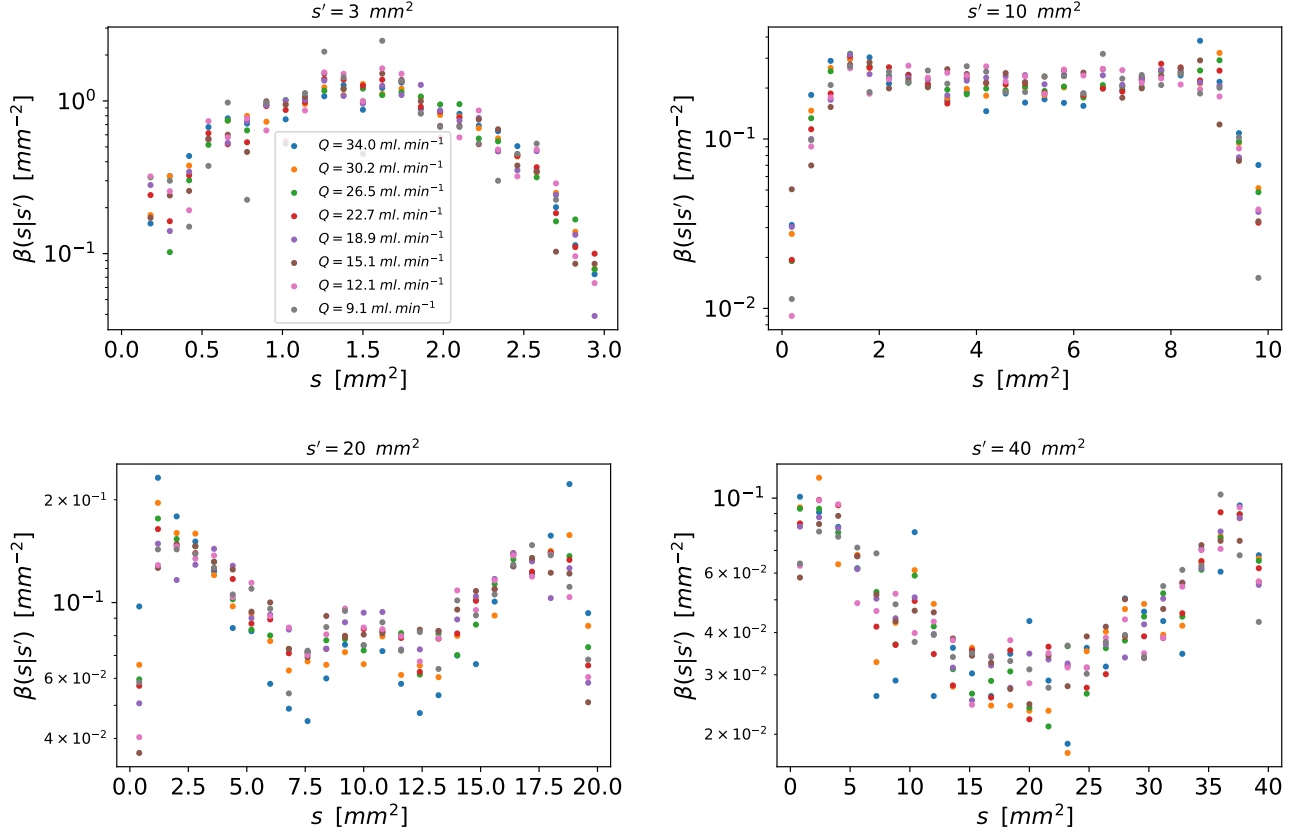


Figure 6. Fragmentation distribution functions, $\beta(s|s')$: the distribution of children blobs of size s resulting from the fragmentation of a parent of size s' . The different numbers correspond to different s' and the symbols correspond to different flow rate Q .

C. Coalescence dynamics

Similarly, the analysis of the evolution of blobs between an image at time t and an image at time $t + dt$ allows to identify coalescence events. Fig. 7 (left) shows the coalescence events that occurred during one experiment (~ 15 min) at $Q = 22.7$ ml/min. Here, each point correspond to the pair of parents (s_1, s_2) that merge to form a new blob of size $s_1 + s_2$. It is interesting to note here that the event region is quite circular and centered in the middle. Again, this is due to the fact that the blob size density has a maximum.

The calculation of the coalescence frequency, $K(s_1, s_2)$ (between an s_1 -sized and an s_2 -sized parent), is based on eq. (4). This equation requires dividing a relatively noisy signal $N^{coal}(s_1, s_2)$ by two other noisy signals $\rho(s_1)$ and $\rho(s_2)$. Therefore, the function $K(s_1, s_2)$ also has significant noise, while the collision frequency is expected to be more accurate in the range where there is large population of blobs (*e.g* $s \simeq 2$ mm²). Fig. 7 (right) shows the resulting $K(s_1, s_2)$ function. Despite the noise, the figure shows

the expected trend that the coalescence probability significantly increases with the size of the two parent blobs.

In order to implement this result in the context of the population balance equation (3), we first need to determine the precise dependence of $K(s_1, s_2)$ on the sizes s_1 and s_2 . In this direction, different functions have been proposed in the literature [37, 38] to model a coalescence process. The most popular functions are either independent of the size of the parent $K = \text{Constant}$, proportional to the size of the final blob $K(s_1, s_2) \propto (s_1 + s_2)$ or proportional to the product of the sizes of the parents, $K(s_1, s_2) \propto s_1 s_2$. In our study, the most satisfactory fit to the experimental results comes from $K(s_1, s_2)$ function of the product of the parent sizes, $K(s_1 s_2)$. In Fig. 8 (top), we thus plot $K(s_1, s_2)$ as a function of $s_1 s_2$ for a given flow rate on a log-log scale. Despite the large scatter, the data exhibits a power-law-like trend that can be averaged. The averaged trend is represented by the red stars in this figure. Fig. 8 (bottom left) displays this average function for different flow rates. The trend is similar for all experiments but the frequency of coalescence increases with the flow rate. The dependence with the flow rate is determined by Fig.8 (bottom right) that shows a reasonable fitting for all data once the frequency is normalized with $Q^{0.8}$, with the notable exception of the two higher flow rates. A careful review of the results reveals that, at high flow rate, coalescence events between larger blobs are rarer (due to overall swift of the population towards smaller sizes). Therefore our averaging and fitting is less accurate under such conditions.

In summary, the coalescence frequency in our experimental setup follows the following scaling:

$$K(s_1, s_2) \propto Q^{\alpha_2} (s_1 s_2)^\chi, \quad (12)$$

with $\alpha_2 \simeq 0.8 \pm 0.2$ and $\chi \simeq 0.4 \pm 0.1$.

From the exponent α_2 , we obtain the expected result that the higher the flow rate, the higher the coalescence frequency. However, since $\alpha_1 > \alpha_2$, the fragmentation rate increases faster than the coalescence rate with Q . Considering the exponent χ , despite the large statistical error, it is not unreasonable to postulate that it would be close to 0.5. This would mean that the collision probability is proportional to the diameter of the blobs (or to an effective cross section).

D. Population Balance Dynamics

In this contribution, we focus on the 'dynamics' of the blob size distribution under steady-state conditions. Therefore, in the context of the mean field approach of Eq. (3) the transient term is equal to zero, i.e. $\frac{\partial \rho(s)}{\partial t} = 0$. The density distribution $\rho(s)$ is thus determined by the dynamic equilibrium among the

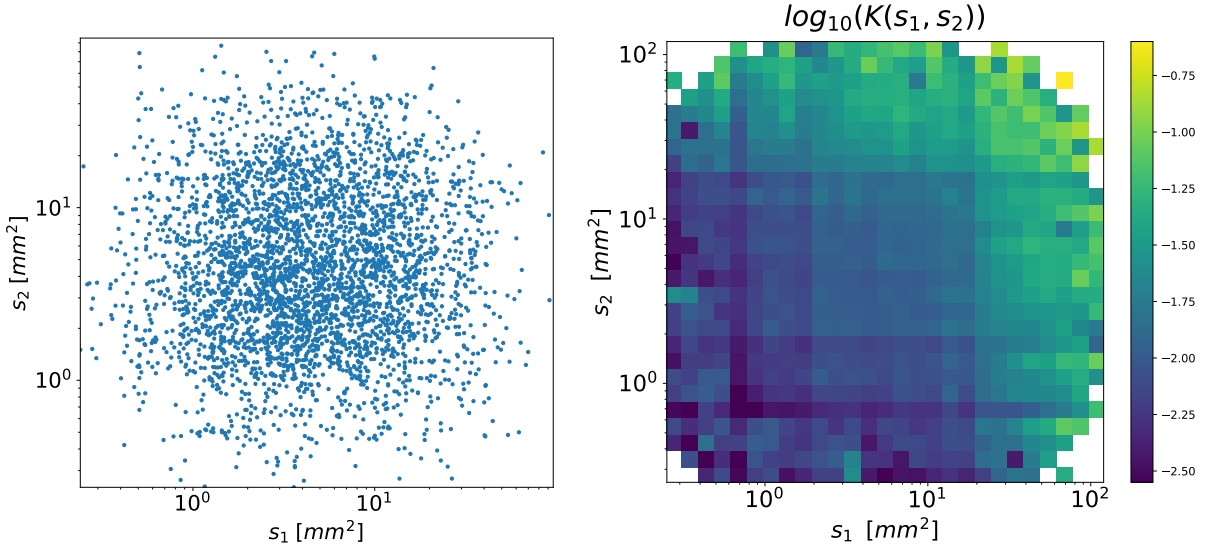


Figure 7. Left: cloud map of the coalescence event during the experiment (~ 15 min) for $Q = 22.7 \text{ ml.min}^{-1}$. Each point correspond to a coalescence of a blob of size s_1 with another blob of size s_2 . There are around 90,000 coalescence events but only 2,000 are displayed. Right: color-map of the corresponding frequency function $K(s_1, s_2)$.

four terms describing the gains and losses by fragmentation and coalescence as follows:

$$\frac{\delta \rho_{gain}^{coal}}{\delta t} = \frac{1}{2} \int_0^s \rho(s-s', t) \rho(s', t) K(s-s', s') ds' \quad (13)$$

$$\frac{\delta \rho_{loss}^{coal}}{\delta t} = - \int_0^\infty \rho(s, t) \rho(s', t) K(s, s') ds' \quad (14)$$

$$\frac{\delta \rho_{gain}^{frag}}{\delta t} = \int_s^\infty \beta(s|s') \Gamma(s') \rho(s', t) ds' \quad (15)$$

$$\frac{\delta \rho_{loss}^{frag}}{\delta t} = -\Gamma(s) \rho(s, t). \quad (16)$$

In order to provide better insight on the contribution of each of the above terms, we need to plot them against the blob size. To do this, one method would be to calculate the integrals with the above determined functions. A simpler and more accurate approach relies on counting the actual number of events that increase or decrease the number of blobs in a given size interval $[s; s+ds]$ and to average them over the duration of the experiment.

Figure 9 shows the absolute value of the four terms as a function of blob size and for two different flow rates. The most striking aspect of these curves is that the different terms seem to match each other in pairs. Furthermore, for the smaller blobs we observe that one pair of terms is much larger than the other, Therefore, for smaller blobs:

$$s \lesssim 10 \text{ mm}^2, \quad \left| \frac{\delta \rho_{gain}^{coal}}{\delta t} \right| \simeq \left| \frac{\delta \rho_{loss}^{frag}}{\delta t} \right| \ll \frac{\delta \rho_{gain}^{frag}}{\delta t} \simeq \left| \frac{\delta \rho_{loss}^{coal}}{\delta t} \right|. \quad (17)$$

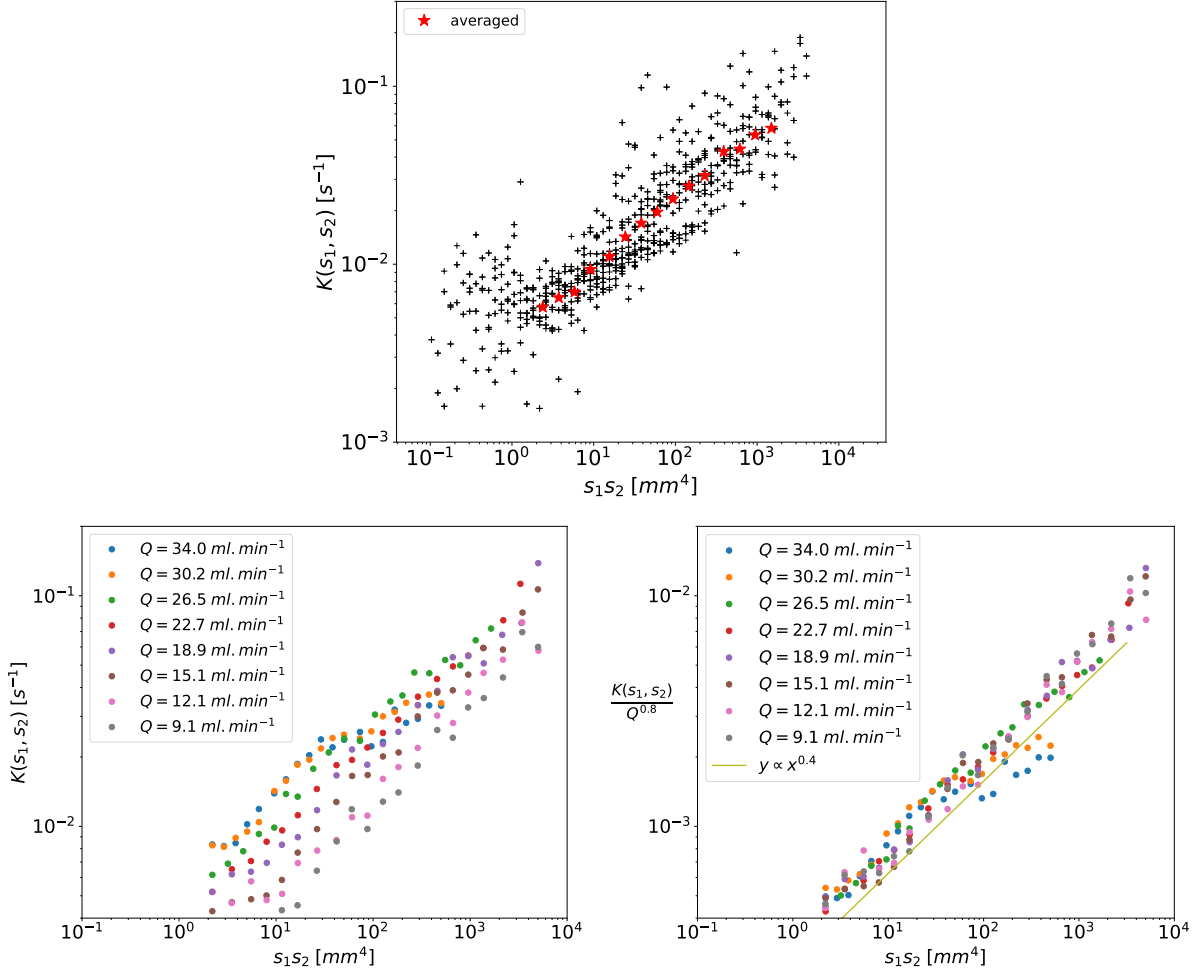


Figure 8. Top: Collision frequency $K(s_1, s_2)$ as a function of the product $s_1 s_2$ for $Q = 22.7 \text{ ml.min}^{-1}$. The red stars correspond to the average for a given $s_1 s_2$. Bottom left: average collision frequency $K(s_1, s_2)$ as a function of $s_1 s_2$ for different flow rates. Bottom right: same curve rescaled with Q^{α_2} , with $\alpha_2 = 0.8$. The green line represents a power-law trend $K(s_1, s_2) \propto (s_1 s_2)^\chi$, with $\chi = 0.4$.

The above result represents the expected much lower probability of smaller blobs to break-up (gain term due to fragmentation of larger blobs). Furthermore, the gain of smaller size blobs by coalescence requires the merging of two even smaller blobs, which is extremely rare.

For a larger blob sizes, we observe that, surprisingly, all four terms seem to have the same order of magnitude. Therefore:

$$s \gtrsim 10 \text{ mm}^2, \quad \left| \frac{\delta \rho_{\text{gain}}^{\text{coal}}}{\delta t} \right| \simeq \left| \frac{\delta \rho_{\text{loss}}^{\text{frag}}}{\delta t} \right| \simeq \frac{\delta \rho_{\text{gain}}^{\text{frag}}}{\delta t} \simeq \left| \frac{\delta \rho_{\text{loss}}^{\text{coal}}}{\delta t} \right|. \quad (18)$$

However, the gain by coalescence (or loss by fragmentation) is always higher than the gain by fragmentation (or loss by coalescence).

The most striking result of the above analysis is certainly the pairwise equality between the terms. It

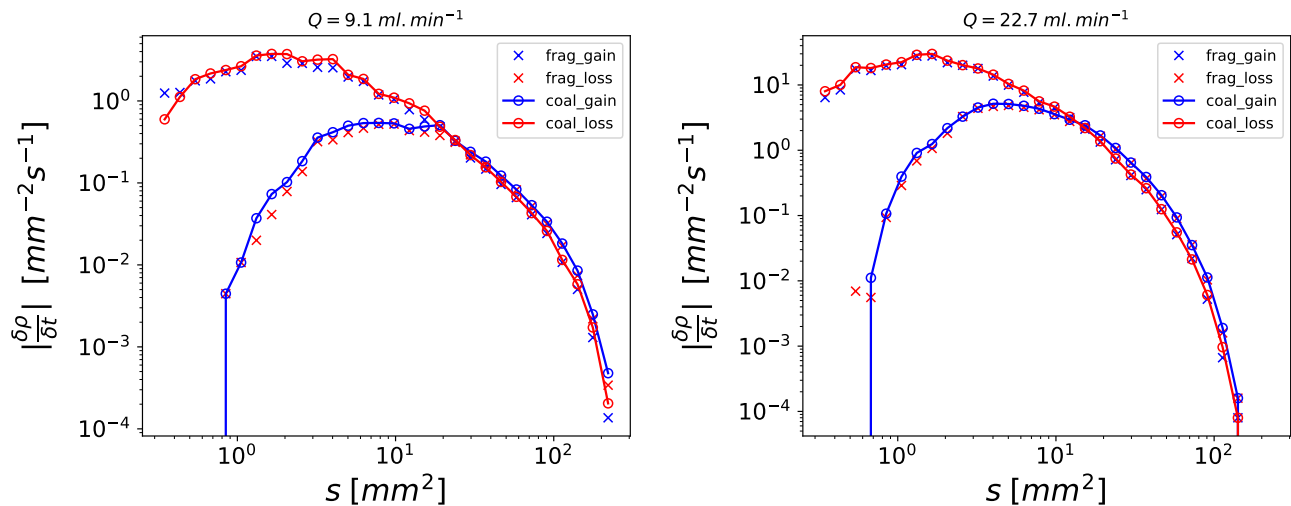


Figure 9. Log-log plot of the four terms involved in the population equilibrium equation as a function of blob size s for two flow rates Q . Circles: Gain (blue) and loss (red) by coalescence. Crosses: gain (blue) and loss (red) by fragmentation.

suggests that, at steady state, the number of s -sized blobs gained by fragmentation is equal to the number lost by coalescence. And the number gained by coalescence is equal to the number lost by fragmentation. A possible explanation for this equality would be that the fragmentation and coalescence events are not independent from each other. One could assume that the fragmentation and coalescence events simply alternate over time. This means that after a fragmentation event the resulting smaller children are more likely to coalesce rather than break-up once again, and after a coalescence event, the new larger blob is more likely to break-up rather than coalesce again, as shown in Fig. 2. In this case, we should expect the mean-field equality between the rate of population gain due to the one type of events and the rate of loss due to the other.

IV. SCALING ANALYSIS AND DISCUSSION

In this work, we were able to identify the different functions that describe the fragmentation and coalescence frequencies. These functions involve power law exponents. From the above mentioned equalities, it is interesting to show that the scaling exponents are not independent. Indeed, from eqs. (16), (8) and (11), we have:

$$\frac{\delta\rho_{loss}^{frag}}{\delta t} = Q^{\alpha_1+\delta+\nu} s^{\gamma_2} g(sQ^\nu) \quad (19)$$

$$\propto Q^{\alpha_1+\delta+\nu-\nu\gamma_2} u^{\gamma_2} g(u), \quad (20)$$

with $u = sQ^\nu$. From eqs. (13), (12) and (8), we have

$$\frac{\delta \rho_{gain}^{coal}}{\delta t} = \frac{1}{2} \int_0^s \rho(s-s')\rho(s')K(s-s',s')ds' \quad (21)$$

$$\propto Q^{\alpha_2+2(\delta+\nu)-2\nu\chi-\nu} \int_0^u g(u-u')g(u')(u-u')^\chi u'^\chi du'. \quad (22)$$

The equality between eq. (16) and (13), therefore implies the relationship between the scaling exponents:

$$\alpha_1 + \delta + \nu - \nu\gamma_2 = \alpha_2 + 2(\delta + \nu) - 2\nu\chi - \nu. \quad (23)$$

And thus:

$$\nu = \frac{\alpha_1 - \alpha_2 - \delta}{\gamma_2 - 2\chi}. \quad (24)$$

Using the measured exponents, it leads to $\nu \simeq 0.67$. Although the agreement is very good with the measured $\nu \simeq 0.7$, it is necessary to stress that this formula is very sensitive to errors. In particular because of the denominator, where there is a subtraction between two numbers of similar magnitude. Despite the fact that the agreement is good, it certainly does not represent a validation because of the large margins of error.

It is also tempting to use the same reasoning to obtain another relationship with eqs. (14) and (15). Unfortunately, the function $\beta(s|s')$ does not have a simple form that allows such a procedure.

Another important point with the scaling with the flow rate, Q , is that we have different exponents for the fragmentation and coalescence frequencies, i.e. $\alpha_1 > \alpha_2$. This shows that, as the flow rate increases, the fragmentation frequency increases faster than the coalescence frequency. This qualitatively explains the evolution of the size density with flow rate (Fig. 3). At high flow rate, the total number of blobs increases while their size decreases because fragmentation is dominant.

We can thus attempt to extrapolate the asymptotic regimes at large and low flow rates. In the limit of large flow rates, coalescence should therefore be negligible and can no longer balance with blob fragmentation. The steady state is thus reached when all the blobs reach the smallest size for fragmentation (the typical pore size). This is for instance the case in the foam fragmentation by Dollet *et al.* [43], where there is no coalescence.

In the opposite limit, $Q \rightarrow 0$, the coalescence becomes dominant and the fragmentation could be neglected. It is now interesting to notice that because we have measured $\chi < 0.5$, we are in the "non-gelling" case as predicted by van Dongen and Ernst for the coalescence only PBE equation [45]. In this case, the blob size distribution solution of the PBE equation, without the fragmentation terms, should converge to a power law eq. (2) with an exponent $\beta = 2$. This would thus potentially explain why this exponent of ~ 2 is observed in many experiments in quasi-static flow condition, which is also very close to that of percolation prediction.

V. CONCLUSIONS

In this contribution, we have performed a pore-scale experimental study in order to investigate the mean-field dynamics of non-wetting phase blobs during immiscible two-phase flow in porous media under steady state conditions. We have applied a clustering algorithm that identifies and correlates the sizes of parent and children blobs during fragmentation and coalescence events. We have demonstrated that the steady-state blob size distribution results from the balance between these two types of events by approximating the analytical expressions of the three functions involved in the population balance equations and by determining their scaling with the total flow. We conclude that the frequencies of fragmentation and coalescence both increase with flow rate but with a different scaling exponent. Furthermore, both frequencies were found to increase with the size of the blob following a power law scaling. The fragmentation rate exhibits a change in the power law exponent at smaller sizes. Regarding coalescence, our results support the argument that the frequency increases with the product of the blob sizes to a power near 0.5.

Several comments can be made. For the sake of simplicity, we have analyzed our results using a fairly simple version of the PBE. But, as discussed in the introduction, one could expect different mechanisms of break-up. In principle, this could imply the need to define different fragmentation probability functions, possibly with different scaling. Here, the data seem to scale relatively well, suggesting that one mechanism is more dominant than the others. Another possibility would be that all mechanisms have the same scaling, which seems rather unlikely.

A more than interesting outcome result of our work is certainly related to the calculated flux balance between the different terms of the blob size population. We observed that the population gain due to fragmentation (resp. coalescence) is equal to the population loss by coalescence (resp. fragmentation) over a narrow region of blob sizes. At first sight, one could compare this to a detailed balance as described by [46], but the comparison is difficult because the detailed balance involves the transition probabilities between different states of a system and each blob cannot really be defined as a state.

We postulate that that this equality results from an alternation between the two types of events, as shown in Fig. 2. After a fragmentation event, breakup, the resulting smaller children blobs are more likely to coalesce than break-up once again, and thus the number of population losses by fragmentation becomes equal the population gain by coalescence on a time-averaged basis.

The results of this work offer a solid basis for further investigating the effects of viscosity and the capillary number on the population dynamics, e.g. by considering a different pair of fluids. It should also be noted that coalescence is also affected by the type of fluid. The fluids considered here have the property to coalesce very quickly when they are in contact. This does not necessarily occur when using an air-water combination, for instance. It has been observed that the bubbles can touch each other without

necessarily coalescing. In this case, we should recover a scaling close to that of the foams. In this regard, another interesting perspective would be to study the limits at very high or very low flow rates. If the size distribution is determined by the fragmentation-coalescence equilibrium, it would be interesting to analyze how this distribution evolves when one of the two types of events becomes negligible.

Acknowledgements. — This work was partly supported by the Research Council of Norway through its Center of Excellence funding scheme, project number 262644. Further support, also from the Research Council of Norway, was provided through its INTPART program, project number 309139. We would like to thank the anonymous reviewers for their insightful comments.

-
- [1] R. Hilfer, “Macroscopic equations of motion for two-phase flow in porous media,” *Phys. Rev. E* **58**, 2090–2096 (1998).
- [2] K. T. Tallakstad, G. Løvoll, H. A. Knudsen, T. Ramstad, E. G. Flekkøy, and K. J. Måløy, “Steady-state, simultaneous two-phase flow in porous media: An experimental study,” *Phys. Rev. E* **80**, 036308 (2009).
- [3] A. G. Yiotis, L. Talon, and D. Salin, “Blob population dynamics during immiscible two-phase flows in reconstructed porous media,” *Phys. Rev. E* **87**, 033001 (2013).
- [4] T. Chevalier, D. Salin, L. Talon, and A. G. Yiotis, “History effects on nonwetting fluid residuals during desaturation flow through disordered porous media,” *Phys. Rev. E* **91**, 043015 (2015).
- [5] S. Sinha, A. T. Bender, M. Danczyk, K. Keepseagle, C. A. Prather, Joshua M. Bray, L. W. Thrane, J. D. Seymour, S. L. Codd, and A. Hansen, “Effective rheology of two-phase flow in three-dimensional porous media: Experiment and simulation,” *Transp. Porous Media* **119**, 77–94 (2017).
- [6] A. G. Yiotis, A. Dollari, M. E. Kainourgiakis, D. Salin, and L. Talon, “Nonlinear Darcy flow dynamics during ganglia stranding and mobilization in heterogeneous porous domains,” *Phys. Rev. Fluids* **4**, 114302 (2019).
- [7] Y. Zhang, B. Bijeljic, Y. Gao, Q. Lin, and M.J. Blunt, “Quantification of nonlinear multiphase flow in porous media,” *Geophysical Research Letters* **48**, e2020GL090477 (2021), e2020GL090477 2020GL090477, <https://agupubs.onlinelibrary.wiley.com/doi/pdf/10.1029/2020GL090477>.
- [8] K.M. Ng, H.T. Davis, and L.E. Scriven, “Visualization of blob mechanics in flow through porous media,” *Chemical Engineering Science* **33**, 1009–1017 (1978).
- [9] A. C. Payatakes, K. M. Ng, and R. W. Flumerfelt, “Oil ganglion dynamics during immiscible displacement: Model formulation,” *AIChE J.* **26**, 430 (1980).
- [10] R.G. Larson, H.T. Davis, and L.E. Scriven, “Displacement of residual nonwetting fluid from porous media,” *Chemical Engineering Science* **36**, 75–85 (1981).
- [11] N. C. Wardlaw and M. Mckellar, “Oil blob populations and mobilization of trapped oil in unconsolidated packs,” *The Canadian Journal of Chemical Engineering* **63**, 525–532 (1985),.
- [12] S. S. Datta, J.-B. Dupin, and David A. Weitz, “Fluid breakup during simultaneous two-phase flow through a three-dimensional porous medium,” *Physics of Fluids* **26**, 062004 (2014),.

- [13] D. G. Avraam and A. C. Payatakes, “Flow regimes and relative permeabilities during steady-state two-phase flow in porous media,” *Journal of Fluid Mechanics* **293**, 207–236 (1995).
- [14] D. Wilkinson and J. F. Willemsen, “Invasion percolation - a new form of percolation theory,” *Journal of Physics A-mathematical and General* **16**, 3365–3376 (1983).
- [15] A.C. Payatakes and M. M. Dias, “Immiscible microdisplacement and ganglion dynamics in porous media,” *Reviews in Chemical Engineering* **2**, 85–174 (1984).
- [16] P. Meakin, G. Wagner, J. Feder, and T. Jøssang, “Simulations of migration, fragmentation and coalescence of non-wetting fluids in porous media,” *Physica A: Statistical Mechanics and its Applications* **200**, 241–249 (1993).
- [17] P.-G. de Gennes and E. Guyon, “Lois générales pour l’injection d’un fluide dans un milieu poreux aléatoire,” *J. Mec* **17**, 403–432 (1978).
- [18] R. Lenormand and C. Zarcone, “Invasion percolation in an etched network: Measurement of a fractal dimension,” *Phys. Rev. Lett.* **54**, 2226–2229 (1985).
- [19] D. Wilkinson, “Percolation effects in immiscible displacement,” *Phys. Rev. A* **34**, 1380–1391 (1986).
- [20] D. Stauffer and A. Aharony, *Introduction to percolation theory* (Taylor and Francis, 1991).
- [21] G. Wagner, A. Birovljev, P. Meakin, J. Feder, and T. Jøssang, “Fragmentation and migration of invasion percolation clusters: Experiments and simulations,” *Phys. Rev. E* **55**, 7015–7029 (1997).
- [22] T. Pak, I. B. Butler, S. Geiger, M.I.J. Van Dijke, and K. S. Sorbie, “Droplet fragmentation: 3d imaging of a previously unidentified pore-scale process during multiphase flow in porous media,” *Proceedings of the National Academy of Sciences* **112**, 1947–1952 (2015).
- [23] M. Rücker, S. Berg, R. T. Armstrong, A. Georgiadis, H. Ott, A. Schwing, R. Neiteler, N. Brussee, A. Makurat, L. Leu, *et al.*, “From connected pathway flow to ganglion dynamics,” *Geophysical Research Letters* **42**, 3888–3894 (2015).
- [24] R. T. Armstrong, J. E. McClure, M. A. Berrill, M. Rücker, S. Schlüter, and S. Berg, “Beyond darcy’s law: The role of phase topology and ganglion dynamics for two-fluid flow,” *Phys. Rev. E* **94**, 043113 (2016).
- [25] J.G. Roof, “Snap-off of oil droplets in water-wet pores,” *Soc Petrol Eng J* **10**, 85–90 (1970).
- [26] J. A. F. Plateau, *Statique expérimentale et théorique des liquides soumis aux seules forces moléculaires*, Vol. 2 (Gauthier-Villars, 1873).
- [27] Lord Rayleigh *et al.*, “On the capillary phenomena of jets,” *Proc. R. Soc. London* **29**, 71–97 (1879).
- [28] D. Salin and L. Talon, “Revisiting the linear stability analysis and absolute-convective transition of two fluid core annular flow,” *Journal of Fluid Mechanics* **865**, 743–761 (2019).
- [29] L. Salkin, L. Courbin, and P. Panizza, “Microfluidic breakups of confined droplets against a linear obstacle: The importance of the viscosity contrast,” *Phys. Rev. E* **86**, 036317 (2012).
- [30] S. Protière, M. Z. Bazant, D. A. Weitz, and H. A. Stone, “Droplet breakup in flow past an obstacle: A capillary instability due to permeability variations,” *EPL (Europhysics Letters)* **92**, 54002 (2010).
- [31] M. V. Smoluchowski, “Drei Vortrage uber Diffusion, Brownsche Bewegung und Koagulation von Kolloidteilchen,” *Zeitschrift fur Physik* **17**, 557–585 (1916).

- [32] P. G. F. Saffman and J. S. Turner, “On the collision of drops in turbulent clouds,” *Journal of Fluid Mechanics* **1**, 16–30 (1956).
- [33] A. M. Golovin, “The solution of the coagulation equation for raindrops. Taking condensation into account,” in *Soviet Physics Doklady*, Vol. 8 (1963) p. 191.
- [34] E. Villermaux, “Fragmentation,” *Annual Review of Fluid Mechanics* **39**, 419–446 (2007),.
- [35] T. Vicsek and F. Family, “Dynamic scaling for aggregation of clusters,” *Phys. Rev. Lett.* , 1669–1672 (1984).
- [36] F. Family, P. Meakin, and J. M. Deutch, “Kinetics of coagulation with fragmentation: Scaling behavior and fluctuations,” *Phys. Rev. Lett.* **57**, 727–730 (1986).
- [37] R. D. Vigil and R. M. Ziff, “On the stability of coagulation—fragmentation population balances,” *Journal of Colloid and Interface Science* **133**, 257–264 (1989).
- [38] S. Kumar and D. Ramkrishna, “On the solution of population balance equations by discretization—i. a fixed pivot technique,” *Chemical Engineering Science* **51**, 1311–1332 (1996).
- [39] This notation has been chosen following [38], but the function $\Gamma(s)$ should not be confused with the special Gamma function.
- [40] A. C. Payatakes, “Dynamics of oil ganglia during immiscible displacement in water-wet porous media,” *Annual Review of Fluid Mechanics* **14**, 365–393 (1982),.
- [41] M. M. Dias and A. C. Payatakes, “Network models for two-phase flow in porous media part 2. motion of oil ganglia,” *J. Fluid Mech.* **164**, 337–358 (1986).
- [42] M. S. Valavanides, G. N. Constantinides, and A. C. Payatakes, “Mechanistic model of steady-state two-phase flow in porous media based on ganglion dynamics,” *Trans. Porous Media* **30**, 267 (1998).
- [43] B. Géraud, Y. Méheust, I. Cantat, and B. Dollet, “Lamella division in a foam flowing through a two-dimensional porous medium: A model fragmentation process,” *Phys. Rev. Lett.* **118**, 098003 (2017).
- [44] B. Géraud, S. A. Jones, I. Cantat, B. Dollet, and Y. Méheust, “The flow of a foam in a two-dimensional porous medium,” *Water Resources Research* **52**, 773–790 (2016),.
- [45] P. G. J. Van Dongen and M. H. Ernst, “Scaling solutions of Smoluchowski’s coagulation equation,” *Journal of Statistical Physics* **50**, 295–329 (1988).
- [46] N. G. Van Kampen, *Stochastic processes in physics and chemistry*, Vol. 1 (Elsevier, 1992).

Appendix A: Identification of the fragmentation and coalescence events

In this section, we describe the algorithm used to identify the coalescence and fragmentation. The first step consists in identifying the blob. First we threshold the blue channel in the video. For each picture, we use a Hoshen-Kopelman algorithm to identify all the connected cluster and to attribute a label for each. The labels between two time sequence are however independent. The idea is to compare the overlap of indices between two images. For instance, Fig. 10 displays the labels for two consecutive times. For instance:

Label 1 at t overlaps with 12 at $t + 1$

Label 2 at t overlaps with 8 and 9 at $t + 1$

Label 3 at t overlaps with 10 at $t + 1$

Label 4 at t overlaps with 13 at $t + 1$

..etc.

It thus identifies the fragmentation of blob 2 and the two resulting children 8 and 9. Similarly, comparing time $t - 1$ and time t allows to identify the coalescence events. Because the algorithm is automatic, other subroutine are implemented to check the conservation of mass. Similarly, events where one blob is partially outside the region of interest are discarded.

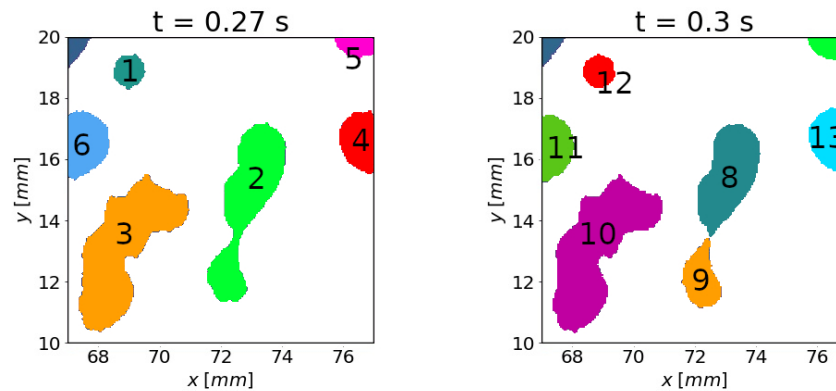


Figure 10. Description of the algorithm. At each time step, a labeling clustering algorithm is applied. The comparison between two images allows to identify fragmentation and coalescence events. Here, the drop labeled 2 at time $t = 0.13$ s overlaps with two labels at the next time. It has thus fragmented to give place to drops labeled 8 and 9 at time $t = 0.17$ s.

Appendix B: Temporal evolution of the number of blobs

In this section we present the time evolution of the total number of blobs, n_T , as a function of time in Fig. 11. The number of blobs follows a stochastic dynamic without any noticeable drift. This confirms that the system is in a steady state during the time range under consideration. The normalised standard deviation for this signal is usually around 0.05.

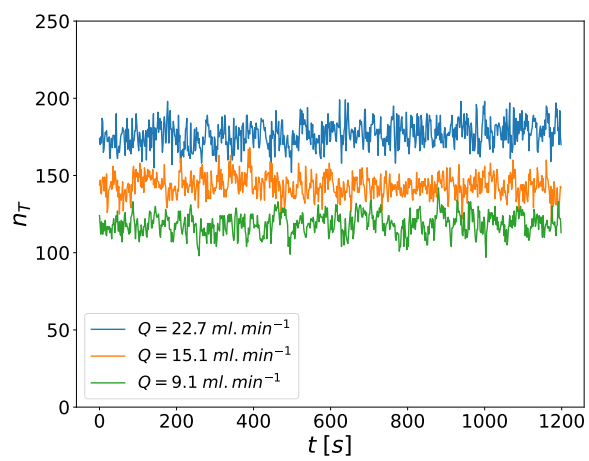


Figure 11. Evolution of the total number of blobs n_T over time for three different total flows Q_T .